Acta Mechanica Sinica (2014) 30(2):259–273
DOI 10.1007/s10409-014-0047-4

RESEARCH PAPER

Multidimensional modeling of the stenosed carotid artery: A novel CAD approach accompanied by an extensive lumped model

A. Kashefi · M. Mahdinia · B. Firoozabadi · M. Amirkhosravi · G. Ahmadi · M.S. Saidi

Received: 28 March 2013 / Revised: 14 May 2013 / Accepted: 11 November 2013

Abstract This study describes a multidimensional 3D/lumped parameter (LP) model which contains appropriate inflow/outflow boundary conditions in order to model the entire human arterial trees. A new extensive LP model of the entire arterial network (48 arteries) was developed including the effect of vessel diameter tapering and the parameterization of resistance, conductor and inductor variables. A computer aided-design (CAD) algorithm was proposed to efficiently handle the coupling of two or more 3D models with the LP model, and substantially lessen the coupling processing time. Realistic boundary conditions and Navier–Stokes equations in healthy and stenosed models of carotid artery bifurcation (CAB) were used to investigate the unsteady Newtonian blood flow velocity distribution in the internal carotid artery (ICA). The present simulation results agree well with previous experimental and numerical studies. The outcomes of a pure LP model and those of the coupled 3D healthy model were found to be nearly the same in both cases. Concerning the various analyzed 3D zones, the stenosis growth in the ICA was not found as a crucial factor in determining the absorbing boundary conditions. This paper demonstrates the advantages of coupling local and systemic models to comprehend physiological diseases of the cardiovascular system.

Keywords Hemodynamic · 3D/LP coupling · CAD · Realistic boundary conditions · Carotid artery bifurcation · Stenosis

A. Kashefi · M. Amirkhosravi
Department of Mechanical Engineering,
Sharif University of Technology, Tehran, Iran

M. Mahdinia
Department of Mechanical Engineering,
University of California Berkeley, Berkeley, USA

B. Firoozabadi (✉) · M.S. Saidi
Faculty of Engineering,
Department of Mechanical Engineering,
Sharif University of Technology, Tehran, Iran
e-mail: firoozabadi@sharif.edu

G. Ahmadi
Faculty of Engineering,
Department of Mechanical and Aeronautical Engineering,
Clarkson University, Potsdam, NY, USA

1 Introduction

According to hematology, the arterial trees in the human body execute biotic functions including the supply of oxygen and essential nutrients to all sites of the body, the transport of hormones and the removal of catabolic products. Computational fluid dynamics (CFD) have been widely used for deeper awareness of diagnosis processes, as well as for better understanding of therapeutic aspects of blood flow in degenerative diseases. The hypotheses of these simulations are typically twofold: first, applying the model of branching arterial trees based on their geometric features frequently to model expanded areas [1–13] and, second, employing localized three-dimensional models explicitly to provide more detailed information [14–21].

From a clinical practice point of view, investigation of blood flow in the carotid artery bifurcation (CAB) is a significant endeavor oriented towards determining the local tissues prone to atherosclerotic lesions. The sinus region of the CAB is believed to have a great propensity to develop these lesions [22]. In this respect, the vascular structure related to localized hemodynamic issues plays an important role in developing stenotic plaques, especially in the region of low wall shear stress [23]. As a consequence, the critical and challenging issue for the formation of this kind of arterial stenosis is to tie its generation to the local flow conditions. However, a better knowledge of the complex flows in this type of vascular region might help in earlier diagnosis of these localized hemodynamic issues.

Numerous researchers have consistently studied CAB using 3D computational flow models [24–28]. Perktold et al. [27] investigated non-stationary non-Newtonian flow characteristics in a 3D CAB model and observed flow separation at the non-divider sinus wall during the systolic deceleration phase. They found that oscillating shear stress throughout the pulse cycle is conclusively generated from the changing of the velocity near the non-divider sinus wall. Ghalichi [29] calibrated the effect of the variation of stenosis in the stenosed model of the CAB under a pulsatile flow simulation and concluded that the stenosis phenomenon could lead to acceleration of the blood flow in the carotid sinus with a high velocity gradient. Also, the author observed forward-directed velocity profiles in the entire stenosis and negative velocities in its downstream. Some computational studies have also been performed in order to suggest a possible explanation of the blood fluid dynamics in the presence of a vascular stenosis [30–34]. In such investigations, the flow and/or pressure pulses as boundary conditions for 3D models were imposed without any feedback from the remaining part of the circulation.

One of the main causes of the problem in precise pressure measurement is the small pressure differences between the inlet and outlet of the investigated territory, in comparison to the systolic-diastolic pulse amplitude. These negligible variations on the actual value of pressure are applied at the inlet and outlet boundaries, which brings about overestimated velocities. Contrarily, trivial errors in the enforced flow could end in considerable deviation in the pressures from the absolute values [35]. On the other hand, analyzing the entire arterial trees as a 3D model could be impractical because of high computational costs and inability to access all of the geometric and physiological information about the blood circulation system. Thus, to efficiently model the global arterial system and substantially decrease the computational expenses, an appropriate approach is to treat localized regions of interest as three-dimensional zones with an LP or one dimensional model of the remainder of the circulatory network leading to realistic boundary conditions.

This geometrical multiscale approach was used by several authors to come to a sufficiently detailed understanding helpful in the treatment of vascular diseases. Laganà et al. [36] linked an LP model with a 3D model to study pulmonary and coronary perfusion in the circulation network. Moura [37] coupled a 3D model of the CAB with a non-artificial 1D vascular system illustrating the circle of Willis and determined that the coupling 3D and 1D fluid-structure interaction (FSI) models could be an accurate tool to gain insight in the vascular systems. Using similar concept, a number of studies have also been reported in Refs. [35, 38–49]. Balossino et al. [38] applied a multidimensional method (3D/LP) to model the three phases of a plaque growth through a real 3D configuration of the CAB with particular role of non-enforced boundary conditions in the prediction of hemodynamics scenarios. Their numerical results showed that stenosis growth in the carotid arteries was significantly dominated by the remaining part of the circulation system, due to lack of noticeable differences between flow rates at the artificial sections of a stenosis carotid artery and a healthy one. Nevertheless, no multiscale investigation on the analysis of physiological blood flow through a stenosis has been reported.

Although numerous studies dealing with the idea of coupling the detailed 1D/3D model with reduced lumped network models have been conducted [36, 38, 50, 51], very few cases are available that have an lumped parameter (LP) model for a considerable number of branches which describes the distributed nature of arterial properties with sufficient accuracy. With a view towards this issue, a multi-segment branching structure consisting of 48 arterial segments was developed in the current study. The effect of vessel diameter tapering and parameterizing the model values to provide the freedom of changing the constituent relations were added to the model, so that one may use the desired relations in place of the ones used previously by Shi et al. [52].

A review of the coupling mechanisms used in geometric multiscale research showed that many previous studies (e.g., Ref. [36]) have taken advantage of the Fluent[1] computational fluid dynamic codes for the 3D portion of the calculations, while they have incorporated relevant governing laws of the entire lumped circulation by including algebraic differential equations in the Fluent code by means of user-defined-functions (UDFs). However, this strategy has come under two major criticisms. First, although adding a UDF to Fluent execution code as a solver of the LP model is a way of obtaining a fully space-time coupled solution, the stringent task of writing UDF code in a parallel platform should be undertaken by users to do parallel 3D computations. Second, derivation of LP model basic equations, transforming the equation system into an ordinary differential equation (ODE) system and finally writing a UDF code in C programming language, all increase the probability of introducing errors. Consequently, most researchers have preferred to use a non-extensive LP model under simplified assumptions. Furthermore, the previous method limits the multiscale model of the cardiovascular system to only one 3D model, whereas coupling two or three detailed 3D simulations with an extended LP modeling of the rest of the cardiovascular system provides a greater opportunity for wider applications.

One of the innovations in the current study is the introduction of an efficient simple computer method on the coupling of 3D and LP models to obviate the noted problems. That is, the LP model was analyzed by means of the Simulink Software in Matlab©, and the Fluent Software was solely used for the 3D parallel computing. More details of

[1] http://www.ansys.com/Products/Simulation+Technology/Fluid+Dynamics/Fluid+Dynamics+Products/ANSYS+Fluent

the analysis are provided in Sect. 2.4. The multiscale model with appropriate LP boundary conditions was applied to a 3D CAB configuration, and the blood flow through this artery with two degrees of asymmetrical stenosis (40% and 55% area reduction) was evaluated. The results are presented in graphical form and discussed.

2 Materials and methods

2.1 The 3D computational model

The standard geometry of CAB, as depicted in Fig. 1a, was taken from data of Bharadvaj et al. [53] and derived from averaging over fifty anatomical different geometries, previously applied by numerous researchers (e.g., Ref. [26]). The common carotid artery (CCA) is 8 mm in diameter (D) and $1.75D$ long. The length of the ICA is assumed to be 5.4 times the diameter of the main branch. This value is equal to 4.1 for the external carotid artery (ECA). The angles between the CCA and the ICA and between the CCA and the ECA are 25° and 28°, respectively. Normal 0%, 40%, and 55% stenosis were considered based on the local diameter as shown in Fig. 2. The aspect ratio, defined as e/D (where e is the extent of the stenosis along the x' axis, see Fig. 1b), was equal to 1.3 for both stenosed models. Five different flow cross-sections ($I_{00}, I_{05}, I_{10}, I_{15}, I_{20}$) in the ICA are considered in Fig. 1b, as done by Gijsen et al. [26]. These appear as reasonable sites to present the velocity distribution. Measuring site I_{00} is located at the flow divider, and other sites were respectively situated downstream of the flow divider by $D/2$ distance along the local axis of the branch (all perpendicular to the x' axis). Here, the x and y velocity components were calculated and subsequently mapped at the x' direction. The designed geometry was investigated to evaluate integrity under assumption of Gijsen et al. [26]. A comparison between experimental and numerical data of Gijsen et al. [26] and the current numerical results is presented in Sect. 3.

Mass and momentum conservation equations were solved using the finite volume method. It is well known that blood can be assumed to be an incompressible, viscous fluid with advantageous Newtonian and laminar behavior in the large blood vessels [34]. Accordingly, the 3D time-dependent Navier–Stokes and the continuity equations are

$$\begin{aligned} &\rho\frac{\partial \boldsymbol{u}}{\partial t} + \rho(\boldsymbol{u}\cdot\nabla)\boldsymbol{u} - \mu\Delta\boldsymbol{u} + \nabla p = \boldsymbol{0}, \\ &\nabla\cdot\boldsymbol{u} = \boldsymbol{0}, \end{aligned} \tag{1}$$

where $\boldsymbol{u}$ and p denote the velocity vector and the absolute pressure at any point in the fluid domain, respectively. A representative blood density value $\rho = 1\,050\,\mathrm{kg/m^3}$ and a typical viscosity $\mu = 0.003\,675\,\mathrm{Pa{\cdot}s}$ were considered. The Reynolds number is given by

$$Re = \frac{\rho D U}{\mu}, \tag{2}$$

where U represents the space-averaged mean CCA flow velocity.

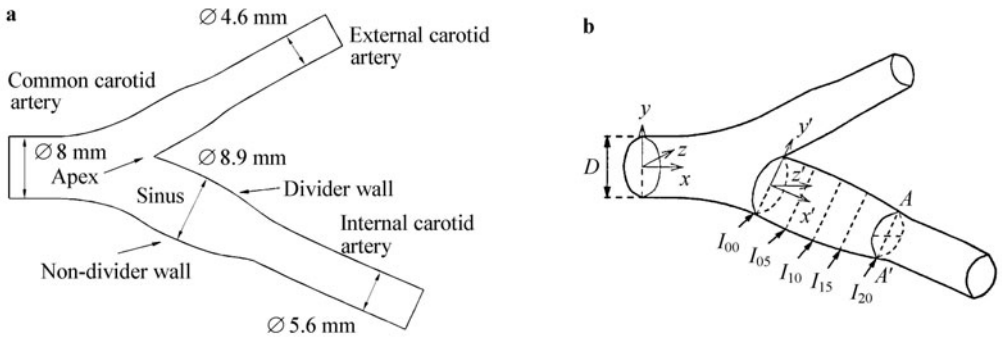

Fig. 1 **a** Schematic representation of the carotid bifurcation; **b** Location of measurement sites

The normal 0%, 40%, and 55% stenosis 3D grids are shown in Fig. 2, with 308 116 nodes and 1 716 445 tetrahedral cells, 374 403 nodes and 1 812 479 cells and 373 802 nodes and 1 810 001 cells, respectively, with very fine grid-spacing near the walls. Time was discretized using the fully implicit backward Euler algorithm, applying a fixed time step equal to 0.002 s. Second-order upwind scheme was utilized for all the equations, and semi-implicit methods were employed for the pressure-linked equation (SIMPLE), coupling the velocity-pressure equations in the CFD calculations. The Green–Gauss node-based technique was chosen as the gradient reconstruction scheme. Momentum and pressure under relaxation factors equal to 0.4 and 0.3 were chosen, respectively. The iteration process at time t^n was considered as converged if the discrete velocity field ($\boldsymbol{u}_h^n$) in the last velocity field iteration process ($\boldsymbol{u}_{h-1}^n$), satisfied the following criterion

$$\left\|\boldsymbol{u}_h^n - \boldsymbol{u}_{h-1}^n\right\| \leqslant r_{\mathrm{res}}, \quad r_{\mathrm{res}} = 10^{-4}$$

with h being the iteration step, r_{res} the residual at iteration, and $\|\cdots\|$ the 2-norm. The arterial walls were treated as rigid boundaries and no slip conditions were imposed.

Cell number and time step sensitivity analysis: Suitable mesh size was selected using the baseline geometry. The average mass flow rate in the ICA outlet section and the velocity profile in I_{10} section at the peak of systole were evaluated for a range of mesh sizes, varying from approximately 800 000 to 2.5 million cells. With regard to the mass flow rate, only fractional differences were observed, and the velocity profile did not change patently when the mesh size was enhanced to more than 1.7 million cells. Moreover, the simulation was accomplished with four fixed time steps of 1×10^{-3}, 1.6×10^{-3}, 2×10^{-3}, and 4×10^{-3} s. Relative errors in the mass flow rate were less than 0.4%, 0.6%, and 1.6% for the last three time step sizes, respectively, when compared to the finest time step case.

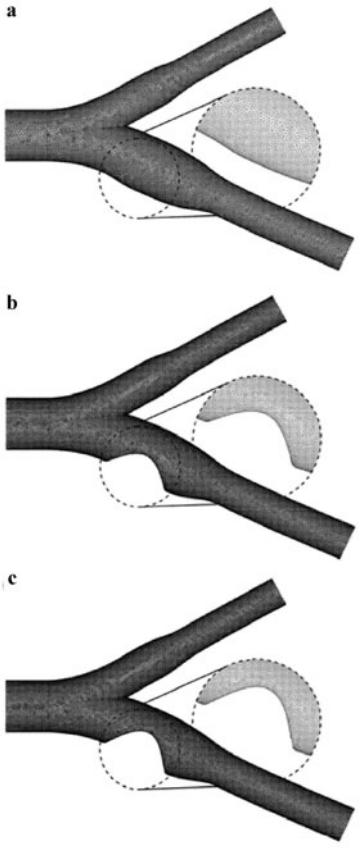

Fig. 2 Representation of the three 3D models used in the simulations. **a** Normal carotid bifurcation; **b** 40% stenosis carotid bifurcation; **c** 55% stenosis carotid bifurcation. Details of the meshes are reported

2.2 The lumped-parameter model

The current study contains a new 48-vessel cardiovascular system which is constructed by following Rideout's [54] methodology. As discussed in Sect. 1, the current model is more compatible with the empirical data in comparison to the previous LP models (see e.g., Refs. [7, 52]), especially considering the following efficient features: parameterizing conveniently the element values to incorporate a fluid's special behavior response (e.g., Newtonian fluid, viscoelastic substance, etc.), linear tapering of the radius along the vein and, finally, initializing the simulation from steady state conditions.

The electrical characteristics of the lumped method are strongly consistent with their physiological counterparts, following these conventions

0.01 mL/Pa (compliance) = 1 μF (capacitance),

1 Pa·s^2/mL (inertia) = 1 μH (inductor),

1 Pa·s/mL (resistance) = 1 kΩ (resistance),

1 mmHg (pressure) = 1 V (voltage),

133 416 mL (volume) = 1 A (charge).

Every artery has been linearly divided into an integer number (n) of compartments on the basis of the ratio of difference between its top radius (r_{top}) and bottom radius (r_{bot}) to its length (l). The collective compartment of each vessel included a pure resistance (R), a conductor (C) and an inductor (L), using π model [54] (see Fig. 4a). The purely viscous resistance (R) is determined as

$$R = \frac{8\mu l}{\pi r^2}, \tag{3}$$

where r represents the local artery radius. The conductor C modeling the vessel restitution behavior is calculated as

$$C = \frac{3\pi r^3 l}{2hE}, \tag{4}$$

where h and E are the wall thickness and elasticity module of the arteries, respectively. The inductor (L) due to blood inertia is given by

$$L = \frac{9\rho l}{4\pi r^2}. \tag{5}$$

The ODE for each compartment is expressed as

$$L\frac{\mathrm{d}I}{\mathrm{d}t} + RI + \frac{1}{C}\int I\mathrm{d}t = V. \tag{6}$$

Here I is the current and V denotes the voltage. For a more detailed description of the implemented lumped methods, one is referred to Refs. [51, 54].

From a computational point of view, the circuit element values could be determined by two strategies: first, using the results obtained by Rideout [54] who used a discrete model to describe the blood flow in cylindrical tubes and, second, applying Eqs. (3)–(5). Table 1 lists the quantities used for atriums, ventricles and pulmonary arteries from the first approach. In addition, arterioles, capillaries and veins have been simulated as one/two separated compartment(s) to simplify the model analysis. The values of the rest of the circulatory system (e.g., carotids, thoracic aorta, hand and foot arteries) were computed based on the second method; geometric and rheology data of arterial segments are shown in Table 2.

Table 1 Quantities used for atriums, ventricles and pulmonary arteries

Vessel name	$R/\mathrm{k}\Omega$	$C/\mu\mathrm{F}$	$L/\mu\mathrm{H}$
Right atrium	0.5	216	0.1
Right ventricle	0.5	145	0.1
Pulmonary artery	1	1	0.1
Pulmonary artery 1	4	3	—
Pulmonary artery 2	8	27	—
Pulmonary vein 1	3	10	—
Pulmonary vein 2	1	10	0.1
Left atrium	0.5	101	0.1
Left ventricle	0.5	25	0.1

The system was solved with the backward Euler method, with a consistency tolerance of 0.000 1. The Simulink software in Matlab© was utilized to execute the novel branching configuration subdivided into six pages exhibited in Fig. 3.

2.3 The coupling algorithm

The coupling scheme between the formulations of two previously mentioned sub-models furnishes a multiscale model of the overall circulation, with appropriately derived realistic boundary conditions at individual domains. Figure 4b gives an illustration of the staggered explicit coupling algorithm. As shown in Fig. 4b, at each time step t^n, the uniform normal total stress at the coupling surfaces of the 3D model is imposed from the solution of the LP model; then, 3D model flow rates at the coupling point boundaries are fed to the LP model at time t^{n+1}.

From the formulation point of view, the whole vessel branching structure can be represented by the electrical components, except on a typical vascular district Ω where the 3D domain is constantly located in time. F_i and p_i ($i = 1, 2, \cdots, n$, indices i and n represent the i-th interface and the total number of interfaces in the 3D model, respectively) denote, respectively, the flow rate and the known value of the instantaneous mean normal pressure through each artificial artery cross-sectional area Γ_i of Ω, as illustrated in Fig. 4b. In this way, F_i can be calculated by

$$F_i(t) = \int_{\Gamma_i} \boldsymbol{u}_\xi \cdot \boldsymbol{n} \mathrm{d}\gamma, \tag{7}$$

where $\boldsymbol{u}_\xi$ is identified as the velocity vector for $\forall \xi \in \Omega$, and $\boldsymbol{n}$ indicates the outward unit normal vector on every Γ_i.

It is worthwhile to note that utilizing a realizable boundary condition is a cumbersome task at the variables that are non-uniformly distributed over the interface structure. Notwithstanding this fact, the prescribed Neumann boundary condition was equipped and justified as the correct choice (as shown in Ref. [51]), expressed as

$$p_\xi \boldsymbol{n} - \mu \nabla \boldsymbol{u}_\xi \cdot \boldsymbol{n} = p_i \boldsymbol{n}, \tag{8}$$

where p_ξ is the hydrostatic pressure at Γ_i. Assuming that the viscosity term is in principle negligible compared to the pressure p_ξ, Eq. (8) can be rewritten as

$$p_\xi = p_i. \tag{9}$$

Notice that the interface conditions described above allow for the possibility of reverse-flow phenomenon at the interface. Further details of this method and its capabilities are also available in Ref. [51].

According to the CFL condition, the time increment of a model should typically be small compared to the time increment of its corresponding higher-dimensional model [37]. However, attempting to optimize the computational cost by choosing the same time steps for both sub-domains is unfeasible, due to the fact that the LP model is solved using an explicit solver and thus requires a much smaller time step. On the other hand, the 3D portion can be extremely costly, specifically due to its complicated three-dimensionality. On this basis, implementing two different time steps for each sub-model requires dealing with the flow time effectively. In this sense, the coupled model is advanced with the smaller time step until the larger one is reached. As a result, a time step of 0.000 001 s was used for the LP model, whereas a time step of 0.002 s was selected for the 3D model. Additionally, cardiac period was 0.8 s.

A computer program was written in Visual Basic to automate the explicit coupling algorithm shown in Fig. 4. Three complete cycles were carried out to achieve a guaranteed stable solution. Every simulation took 98 CPU hours, on average, and calculations were performed on an Intel(R) Core(IM) i7 processor, with a 3.1 GHz clock rate and 12 Gigabytes of RAM, supporting a multi-core parallel simulation.

2.4 Computational implementation method

A schematic of the proposed computational implementation method is given in Fig. 5. This method provides two advantages; first, implementing all utilities of Simulink Software is feasible, including current and voltage diagrams trace in each component of LP model to create a feed-back of the accuracy of coupling process, and automatic solution of π model circuits. In this way, derivation of non-linear algebraic-differential equation system and writing a UDF code in C programming language are avoided. Moreover, the probability of introducing errors has sharply decreased and extension of LP model and modification of each desired component are conveniently carried out. In addition, when there is no need to write the program in C language, consequently, the necessity of adding a UDF to Fluent code (or to other most widely used 3D models simulation software) disappears. Hence, parallel computing can be applied in this method to considerably lessen the simulation process time. Reporting the coupling process time by articles utilizing prevailing methods is not common. Nonetheless, its value can be approximately estimated, considering two hypotheses; first, in the

worse possible case, the real time to solve the LP model at each time step in Simulink Software is equal to the one in the UDF code. Second, simulation of the 3D model is performed only on a single process machine rather than on a parallel one (Notice that this condition is equivalent to applying UDF code in Fluent and the possibility of parallel computation does not exist.). Taking these two hypotheses into account, each simulation takes 720 hours on average (nearly one month), incomparable with 98 hours. Definitely the more the number processes, the less the simulation time.

Table 2 Geometric and rheological properties of the considered arterial segments

No.	Name	n	l/cm	r_{top}/cm	r_{bot}/cm	E/MPa	h/cm
1	Ascending aorta	10	1.00	1.525	1.502	0.4	0.163
2	Coronaries	15	10.00	0.350	0.300	0.4	0.010
3	Ascending aorta	20	3.00	1.502	1.420	0.4	0.163
4	Aortic arch	6	3.00	1.420	1.342	0.4	0.143
5	Brachiocephalic	7	3.50	0.950	0.700	0.4	0.085
7	Right common carotid	5	16.75	0.525	0.400	0.4	0.064
12	Aortic arch	8	4.00	1.342	1.246	0.4	0.124
13	Left common carotid	5	19.25	0.525	0.400	0.4	0.124
14	Thoracic aorta	2	5.50	1.246	1.124	0.4	0.057
15	Thoracic aorta	4	10.50	1.124	0.924	0.4	0.066
16	Intercostals	2	7.25	0.630	0.500	0.4	0.043
17, 6	Subclavian	2	3.50	0.425	0.407	0.4	0.066
18, 8	Vertebral	1	13.50	0.200	0.200	0.4	0.047
19, 9	Left and right brachial	5	39.75	0.407	0.250	0.4	0.043
20, 11	Right and left ulnar	2	22.25	0.175	0.175	0.8	0.064
21, 10	Left and right radial	2	22.00	0.175	0.175	0.8	0.043
22	Celiac axis	2	2.00	0.350	0.300	0.4	0.029
23	Hepatic	2	2.00	0.300	0.250	0.4	0.029
24	Hepatic	2	6.50	0.275	0.250	0.4	0.080
25	Gastric	3	5.75	0.175	0.150	0.4	0.066
26	Splenic	1	5.50	0.200	0.200	0.4	0.080
27	Abdominal aorta	3	5.25	0.924	0.838	0.4	0.080
28	Superior mesenteric	2	5.00	0.400	0.350	0.4	0.043
29	Abdominal aorta	2	1.50	0.838	0.814	0.4	0.080
31	Abdominal aorta	2	1.50	0.814	0.792	0.4	0.080
30, 32	Renal	2	3.00	0.275	0.275	0.4	0.043
33	Abdominal aorta	4	12.50	0.792	0.627	0.4	0.080
34	Inferior mesenteric	2	3.75	0.200	0.175	0.4	0.043
35	Abdominal aorta	3	8.00	0.627	0.550	0.4	0.080
36	External iliac	2	5.75	0.400	0.370	0.4	0.076
37	Femoral	4	14.50	0.370	0.314	0.8	0.048
38	Internal iliac	1	4.50	0.200	0.200	0.4	0.076
39	Deep femoral	1	11.25	0.200	0.200	1.6	0.047
40	Femoral	8	44.25	0.314	0.200	0.8	0.048
41, 42	External and internal carotid	4	15.75	0.275	0.200	0.8	0.052
43, 44	Posterior and anterior tibial	1	32.00	0.125	0.125	1.6	0.038
46, 47	Right and left ulnar	1	17.00	0.200	0.200	0.8	0.047
45, 48	Interosseus	1	7.00	0.100	0.100	0.8	0.023

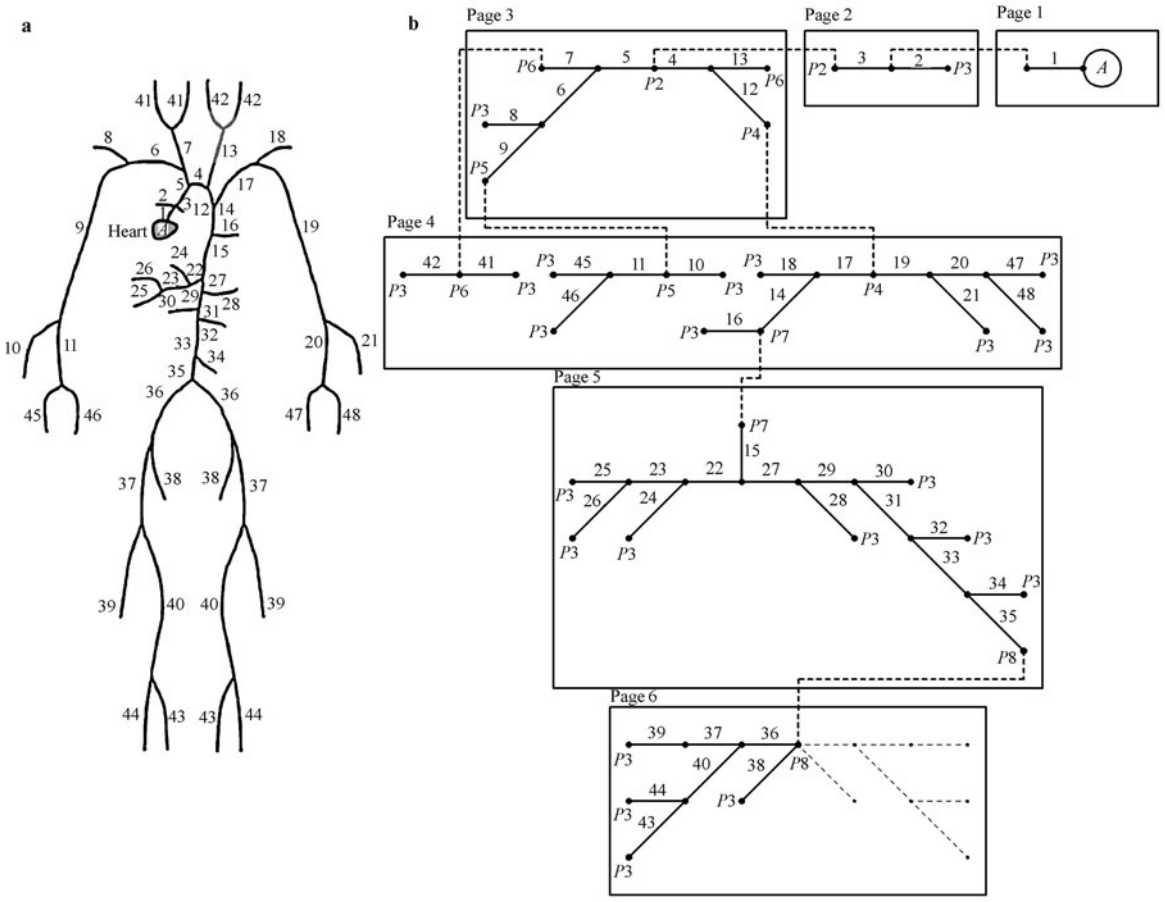

Fig. 3 **a** Arterial tree scheme and **b** schematic representation of the novel branching configuration subdivided into six pages. The human heart model A, is indicated. Pi $(1, 2, \cdots, 8)$ represents potential sites; $P3$ indicates the equivalent potential of capillaries and vein compartments. Any two points with the same potential may be connected by a dashed line

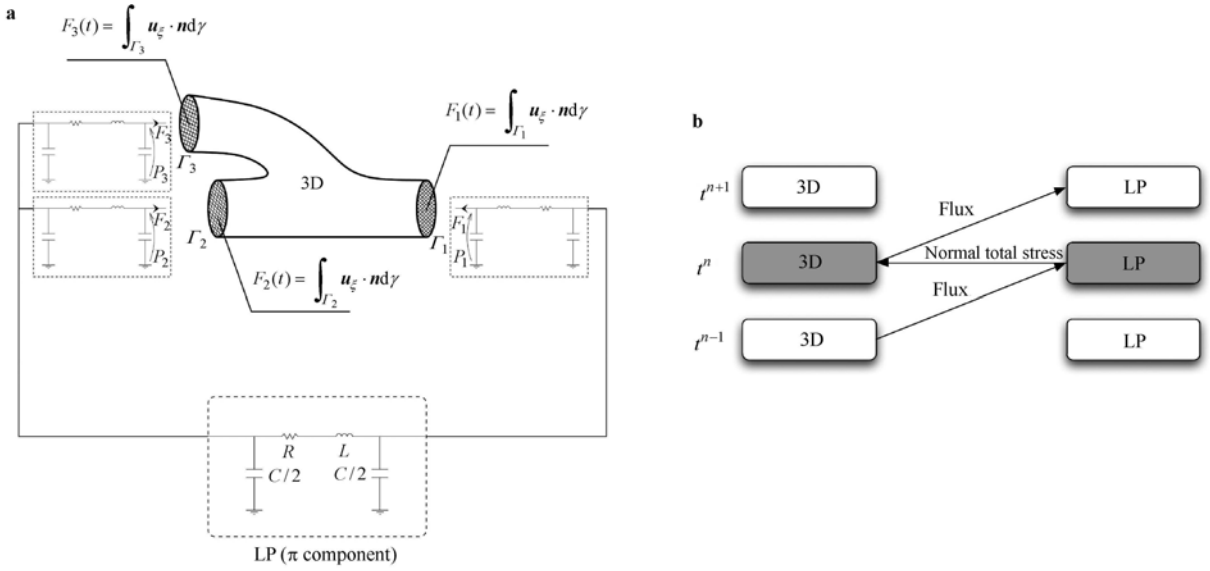

Fig. 4 **a** Explicit coupling of the 3D and LP models; **b** Scheme of coupling between a local district and the whole system, consisting of a resistance R; A conductor C and an inductor L

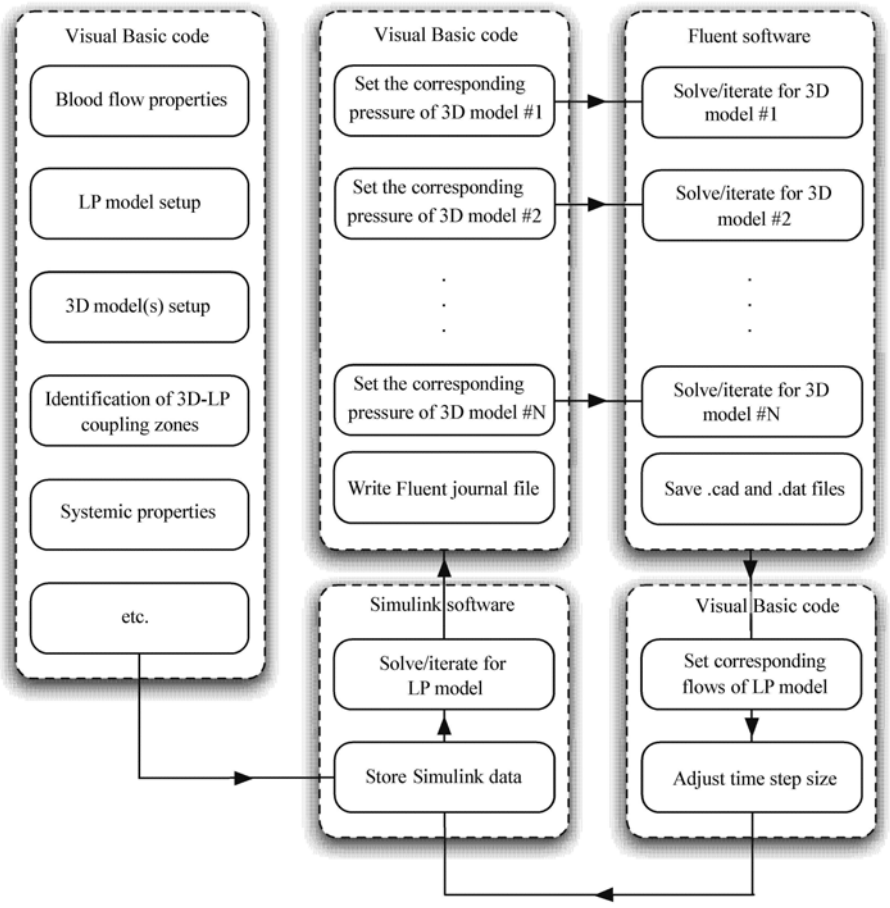

Fig. 5 Block diagram of the proposed computer implementation method

The second advantage is that the proposed method can handle the coupling of more than one 3D model with an extended LP model. This is because of separation of the 3D solver software from that of the LP model. However, the current study focuses on only one 3D model. Visual Basic (VB) code establishes a connection between Simulink Software and Fluent. As can be seen in Fig. 5, the VB code receives the problem inputs (including blood flow properties, systemic properties, LP and 3D model(s) setup, etc.), based on which, at each time step, first runs Simulink Software and then obtains the voltages at artificial boundaries as outputs and inserts specific coefficients to transform them into pressure variables. Having performed this, the VB code creates a "Fluent journal file(s)". This code automatically runs "Fluent case file(s)" by a batch file commands. At this stage, "Fluent case files" are simultaneously run in proportion to the number of 3D models. Fluent code follows the journal file commands. At the end of the time step, it receives the flow rates reported by Fluent, inserts particular coefficients to transform them to electrical currents and assigns them in Simulink software as the next step inputs. This trend continues as shown in Fig. 5 diagram. Since the VB code is written in an object oriented form, it has the potential to connect other software too. For instance, a 1D model simulated by Matlab© can be coupled with a 3D model simulated by Fluent (or any other common 3D models simulation software).

As the first step of a geometrical multiscale application, the 3D simulation starts at a steady state, with boundary conditions imposed from the steady state solution of the non-coupled LP model. Next, the LP and the 3D models are linked together, and the process is smoothly continued in an unsteady state, as shown in the framework of Fig. 5.

3 Results and discussion

3.1 Model verifications

To verify the accuracy of the constructed 3D model, a steady state simulation was performed under assumptions of Gijsen et al. [26]. Figure 6 shows the obtained axial velocity profiles at five different cross-sections in the ICA region for a Reynolds number of 270, revealing good agreement with the experimental and numerical data of Gijsen et al. [26].

The LP model was examined by plotting the blood pressure for the Abdominal aorta, the Internal iliac and the femoral arteries in Figs. 7a–7c, respectively. As can be seen in Fig. 7, at the end of the mid-diastolic phase of a cardiac cycle, the new 48-vessel LP model has more conformity with the 29-vein one-dimensional model of Azer [4] compared to the 36-vessel electrical analog model [7].

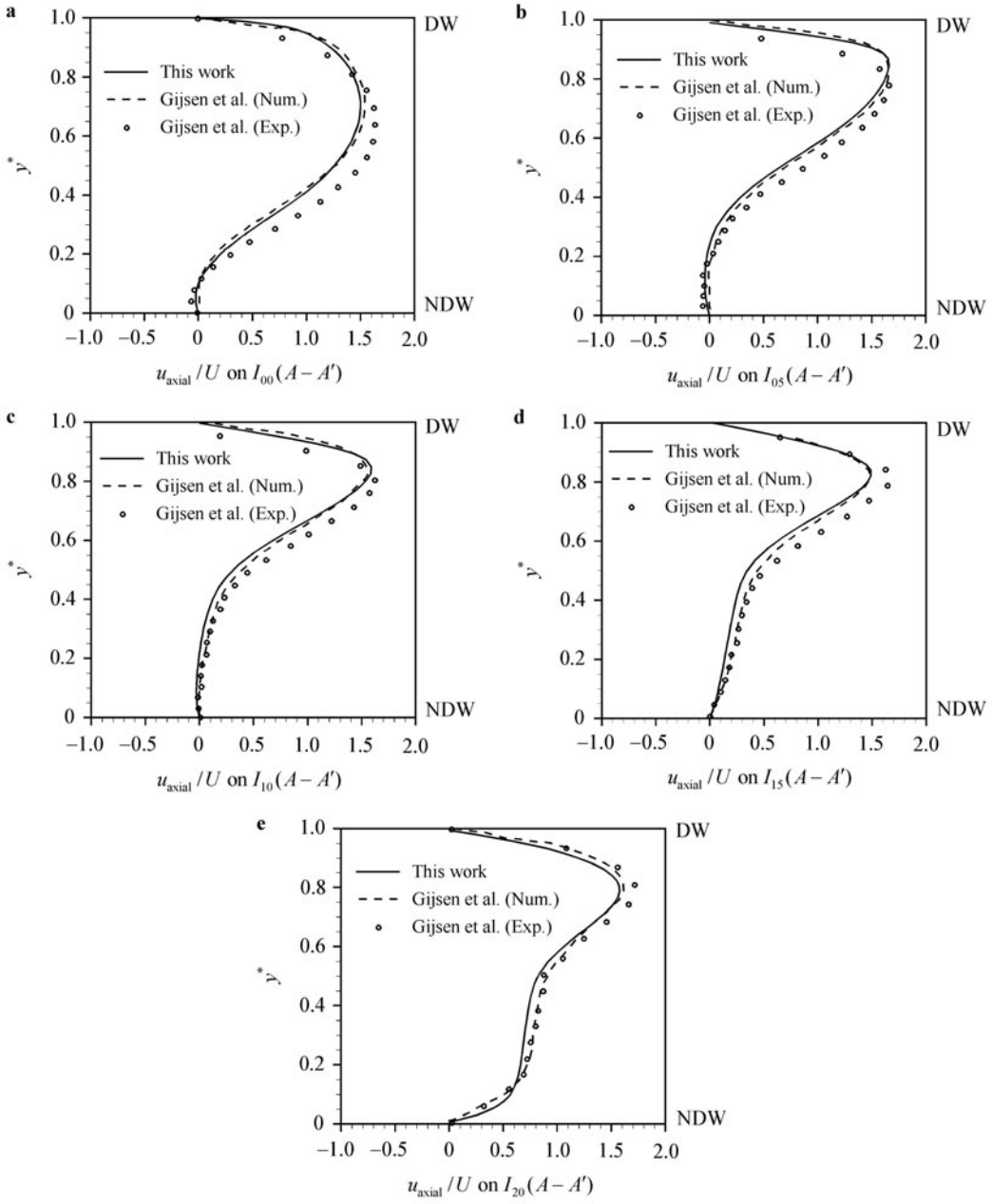

Fig. 6 Axial velocity distribution of the internal carotid artery at various locations of the non-stenosed model. A comparison between Gijsen et al.'s (1999) [26] experimental and numerical data and the current numerical results. U and y^* indicate the mean axial velocity in the common carotid artery and the transverse location, respectively. In addition, the divider wall and non-divider sides are represented by DW and NDW, respectively

In order to show the compatibility of a referenced non-coupled lumped model solution with the multidimensional coupled model, the volumetric flow rate and pressure magnitude at the inlet of 3D region are reported in Fig. 8a; Figures 8b and 8c show the same quantity for both outlets. The analysis of these curves demonstrates that the couple solution is in good agreement with a pure LP model, as expected, and leads to fluctuations lower than 4% for all cases, resulting in only negligible spurious wave reflection. These waves may occur due to reflection from the venous peripheral wall. Here, this effect is diminished by the presence of conductors in the LP model.

3.2 Hemodynamic considerations

In this section, first, the role of the presence of a stenosis in prediction of hemodynamic changes is illustrated by comparing the data for mean flow rates and pressure drops. Next, a more detailed inspection of the flow field is carried out in the sinusoidal region of the investigated 3D models.

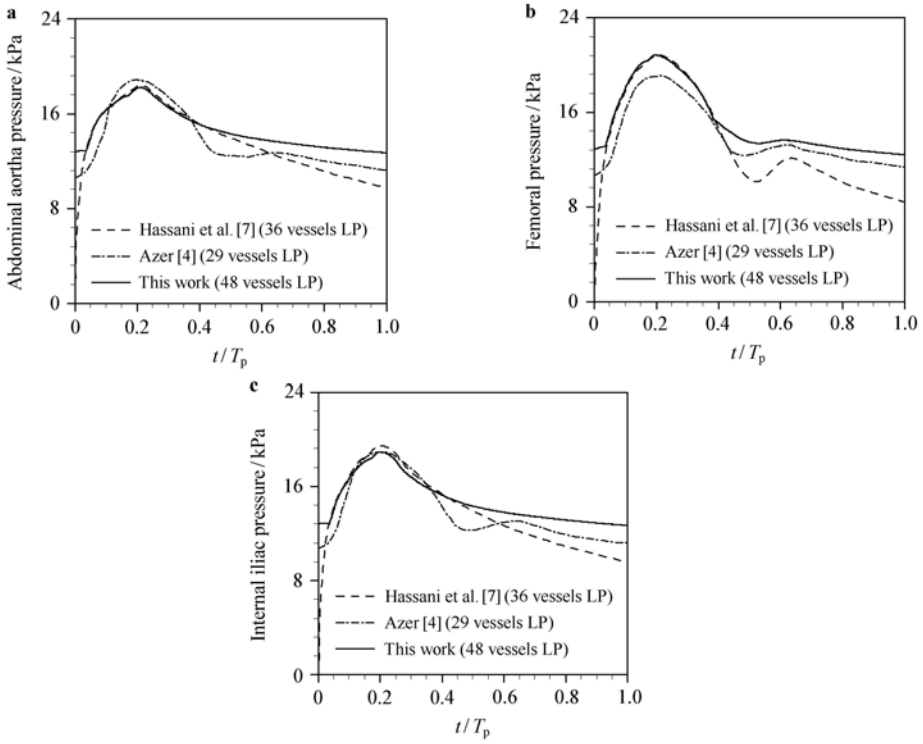

Fig. 7 A comparison between blood pressure of the novel 48 vessel LP model with the 36 vessel electrical analog model [7] and the 29 vein one-dimensional model [4] for **a** abdominal aorta; **b** Internal iliac artery and **c** femoral artery

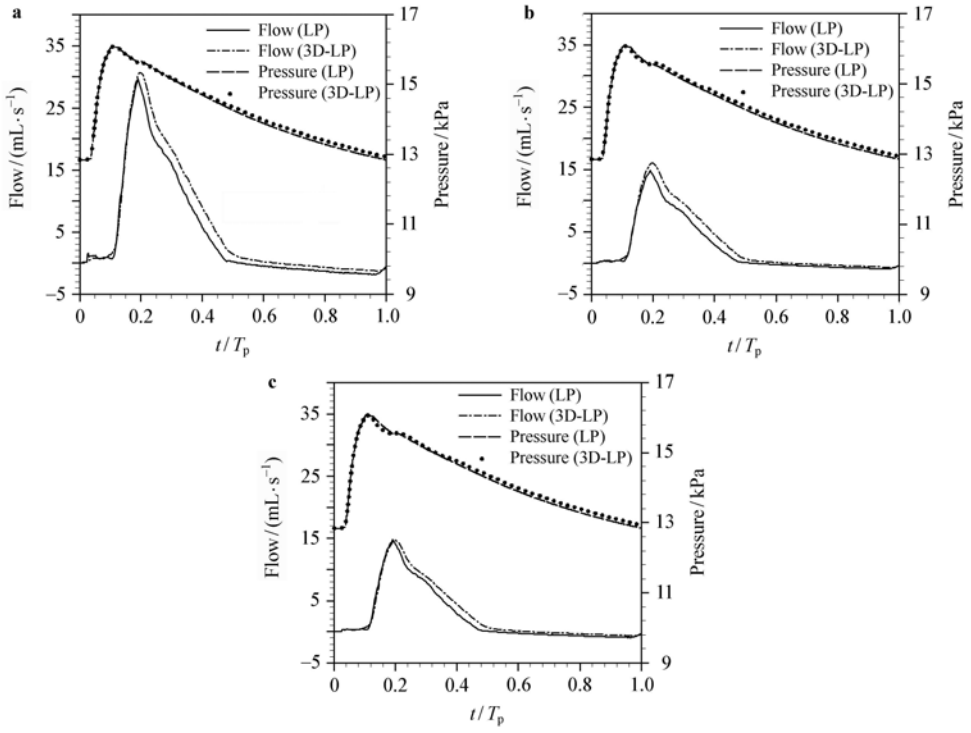

Fig. 8 Comparison between pure LP and coupled 3D-LP flow rates and pressure curves at the interfaces. **a** CCA; **b** ICA; **c** ECA

3.2.1 Realistic boundary conditions

Table 3 summarizes the values of the average flow rates and pressure drops at the interfaces of normal 0%, 40%, and 55% stenosis models. The average CCA volume flow rate slightly decreases with the growth of stenosis (−0.35% and −0.45%, respectively, for 40% and 55% stenosis), which is comparable with the decrease in the mean ICA volume flow rate

(−0.54% and −0.9%, respectively, for 40% and 55% stenosis). Even though the increase in the ECA volume flow rate (+0.03%, for 55% stenosis) compensates the CCA volume flow reduction in the 55% stenosis model, a 0.14% reduction in the ECA volume flow rate is observed in the 40% stenosis case. The reason for the rather small changes in average volume flow rates of the analyzed 3D models may be clear by examining the associated pressure gradients. As it can be seen from Table 3, the presence of a stenosis in the ICA brings about only a slightly larger pressure drop compared to the healthy branch (6.65 vs. 5.32 Pa). This could be in part due to the short length of the ICA and ECA 3D models. According to the study of Balossino et al. [38], choosing greater ICA and ECA length in the 3D models leads to conspicuous pressure gradients in the stenosed branch compared to those in the non-stenosed branch; nevertheless again, the reduction of the flow rate is minute.

Table 3 Comparison of average flow rates and pressures at the interface sections between the study models

Stenosis	$Q_{CCA}/(mL \cdot s^{-1})$	$Q_{ICA}/(mL \cdot s^{-1})$	$Q_{ECA}/(mL \cdot s^{-1})$	ΔP_{ICA}/Pa	ΔP_{ECA}/Pa
0%	5.736	2.981	2.755	5.32	9.31
40%	5.716	2.965	2.751	6.65	10.64
55%	5.710	2.954	2.756	6.65	10.64

Note: Q is flow rate, ΔP is pressure drop

The flow rate temporal tracings during a cardiac cycle at the artificial inlet/outlet sections of the studied models are shown in Fig. 9. As it can be seen in this figure, the differences between the outcomes of the non-stenosed model and those of the 40% or 55% stenosis models are small. Under these circumstances, and in contrast to the expectations, the sensible boundary conditions at the artificial sections do not strongly respond to the stenosis resistance, as the situation changes from healthy case to 40% or 55% stenosis cases. In this regard, the effect of downstream resistance in the 3D geometries does not play a dominant role on the outlying districts. The same observation was also reported by Balossino et al. [38].

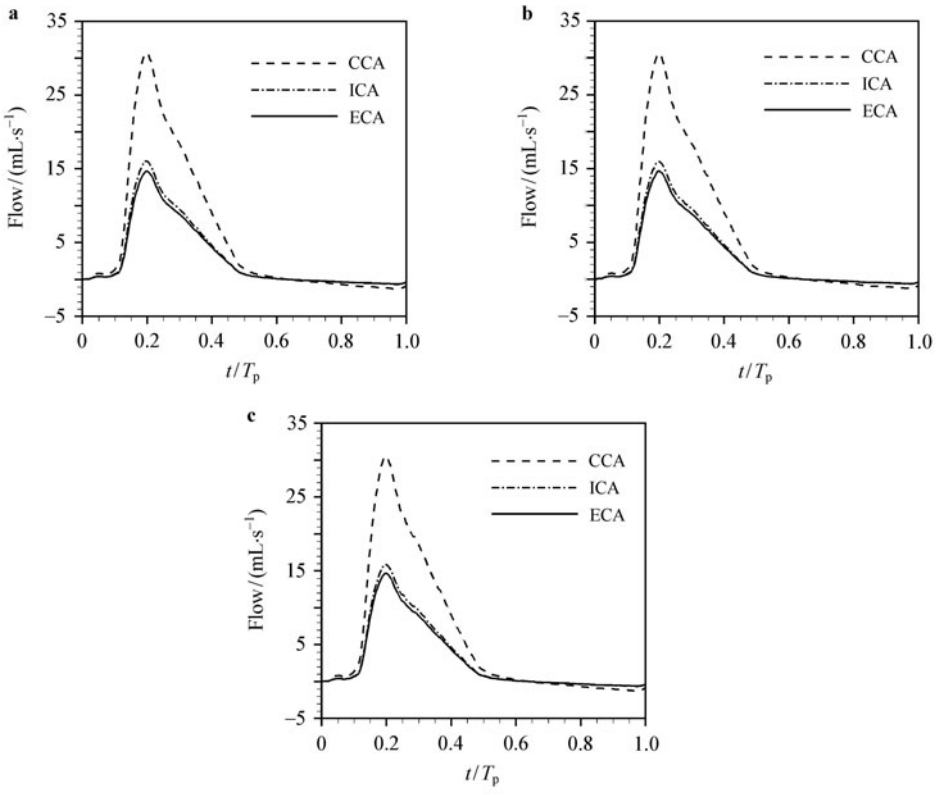

Fig. 9 Coupled 3D/LP flow rate at the inlet/outlet interfaces (CCA, ICA and ECA) for all models under investigation. **a** Normal carotid bifurcation; **b** 40% stenosis carotid bifurcation; **c** 55% stenosis carotid bifurcation

3.2.2 Axial and secondary flow in the carotid sinus

In Fig. 10, the axial velocity profiles in the ICA are given as a function of time during the pulse cycle, including the systolic peak flow (ps, $t/T_p = 0.2$ and $Re = 1\,400$), deceleration phase (dec, $t/T_p = 0.35$ and $Re = 570$) and end systolic flow (es, $t/T_p = 0.55$ and $Re = 55$). These computational results for three models in non-stenosed case and with 40% and 55% stenosis are presented in Figs. 10a–10c, respectively. In general, the blood flow pattern gives an indication of the influence of stenosis development on the genesis of atherosclerotic lesions. A region with flow reversal can be observed in the most proximal part of the carotid sinus in the non-stenosed model, growing intensively beyond the inside and outside parts of the sinusoidal region in the stenosed cases. This reversed flow is absent during peak systole and is slowly developed during the diastolic cycle, which lasts for a longer period of time for the 55% stenosis compared to the 40% stenosis case, as can be seen from the axial velocity lines in Fig. 10. In the systolic peak flow, symmetrical, forwardly directed and flattened axial velocity profiles can be observed in the non-stenosed model. However, these trends are clearly different near sites I_{10} and I_{15} of the stenosis models. In this case, the largest positive axial velocities occur in the 55% stenosis model and reach their maximum values near site I_{10}, mainly due to the decrease of the cross-sectional area. High axial velocity gradients near the divider wall and minute negative axial velocities near the non-divider wall are observed in the deceleration phase at sites I_{00}, I_{10}, and I_{20} for the 40% stenosis model; the same trend is repeated for 55% stenosis. This event was only found at site I_{00} in the healthy model case, most likely due to the curvature effect and flow separation. At the end of the systolic phase, negative axial velocities maintain about the same magnitude as the positive axial velocities. These negative velocities are also observed along the divider wall side at site I_{20}, whereas they were absent in the peak systolic or deceleration phase of the pulse cycle for all 3D models. At this time level, severe velocity gradients are observed near site I_{15} for stenosed models, a result that is not present in the healthy model. Instead, these gradients are found at site I_{00} and I_{05} in the non-stenosed model.

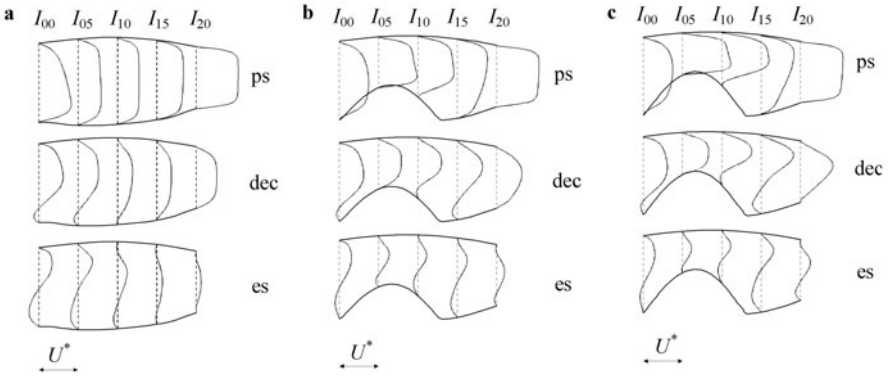

Fig. 10 Axial velocity profiles in the internal carotid artery, present at three times: ps (peak systolic), dec (deceleration) and es (end systolic). **a** Normal carotid bifurcation; **b** 40% stenosis carotid bifurcation; **c** 55% stenosis carotid bifurcation. Maximal axial velocity at peak systole in the common carotid artery (U^*) is indicated

In Figs. 11a–11c, the magnitude of wall shear stress (WSS) distribution was examined along the non-divider wall in the ICA as a model function in non-stenosed case and with 40% and 55% stenosis during the pulse cycle, including the systolic peak flow, deceleration phase and systolic end flow. The maximum absolute value of WSS occurs in the systolic peak flow for all cases, and this parameter sharply decreases during the deceleration phase and systolic end flow. The presence and growth of severe stenosis lead to a high wall shear area inside the stenosis, associated with deposits and atherosclerotic plaque formation, endothelial lining damage and hemodynamic factors alteration in lesion vicinity [29].

Figures 12a–12c depicts the X component of the velocity contour maps at the end of the systolic cycle and identifies the location of the flow recirculation zone, where the flow reversal occurs. Regarding the non-stenosed model, it can be inferred from this figure that the zones of reversed flow are only observed in the carotid sinus and near the non-divider wall. Contrarily, the existence of a stenosis leads to the extension of the recirculation zones towards downstream of the stenosis, which significantly influences the development of early atherosclerotic plaques. Furthermore, as it can be observed in this figure, a typical Womersley flow exists at the entrance of the CCA, where the secondary flow appears at the outer ring, whereas at the center the velocity persists in downstream direction. The results described above are consistent with the general flow pattern found in previous works [28, 29, 35]. Comparison of flow hemodynamic properties between diseased branches and healthy ones may provide useful information for diagnosing arterial diseases.

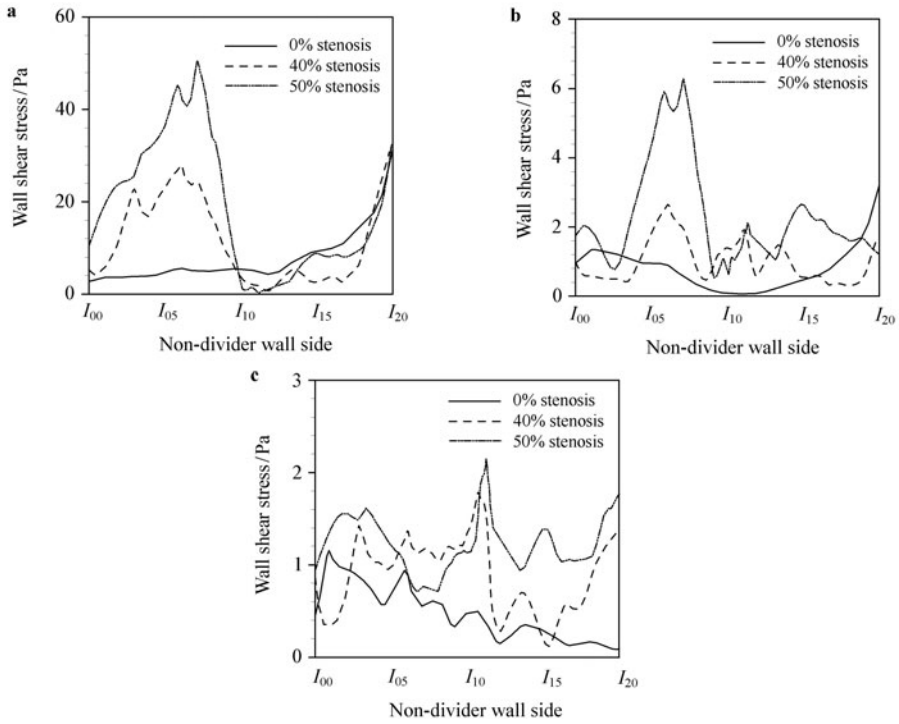

Fig. 11 Wall shear stress distribution along the non-divider wall side on an ICA in three forms: normal carotid bifurcation, 40% stenosis carotid bifurcation and 55% stenosis carotid bifurcation. **a** ps (peak systolic); **b** dec (deceleration); **c** es (end systolic)

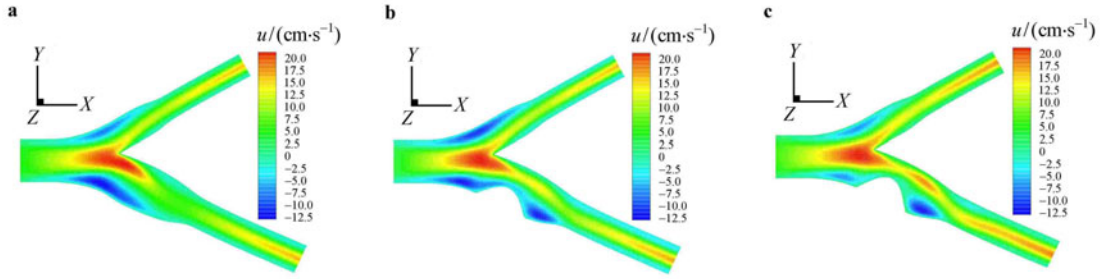

Fig. 12 *X*-velocity component contour at the end of systolic cycle. **a** Normal carotid bifurcation; **b** 40% stenosis carotid bifurcation; **c** 55% stenosis carotid bifurcation

3.3 Future studies

For future studies, two different local 3D domains coupled with the one dimensional model of Reymond et al. [10] for the rest of the arterial trees will be analyzed in order to investigate the influence of an Aortic arch aneurysm on the flow in a patient's CAB, mainly due to the presence of an extensive systemic circulation. Likewise, the implementation of a 3D FSI model instead of a rigid 3D model is being considered to allow detection of local blood flow features. This type of multiscale application will more accurately describe physiological flow patterns and can eventually be used for the prediction of clinical data.

4 Conclusions

The main goal of the present study was the development of a coupling algorithm between local and systemic models, to describe the flow morphology of a specific 3D region of interest more efficiently. A novel CAD scheme was developed and specifically designed to simultaneously couple more than one 3D model with an extensive LP model. As a result, an analysis of examples with two or more 3D elements is being carried out for a future work. Here, the 3D model of a CAB was embedded in a novel lumped network system improving the earlier models cited in the literature [3, 7, 52]. The validity of the presented multiscale scheme was verified and the computed flow rates and pressure drops were compared with the results of an uncoupled LP model, and the importance of the coupling boundary zones was pointed out. Using properly modeled boundary conditions, the flux distributions and time varying velocity profiles at asymmetric stenosis and ideal carotid models were examined. It was shown that the present models simulation results are in general agreement with numerical models reported previously

in the literature [27–29, 35]. Moreover, realistic boundary conditions were identified as independent predictors in the presence of a stenosis in the ICA. In this regard, the computational methodology presented here can help in diagnosing arterial diseases. Furthermore, the described multiscale approach could provide a valuable tool for determining the most important surgical operation parameters, such as the percentage of stenosis and plaque rupture. It may be an effective aid for hematological experts to check the spread of atherosclerotic disease. Finally, the present coupled approach points to the importance of using realistic boundary conditions compared to the classical strategies for studying 3D domains of the blood circulation circuit.

Acknowledgements The authors would like to acknowledge the contributions of K. Allah Verdi to artworks used in the current article. Thanks are given to the Iranian National Science Foundation (INSF) for the financial support to this project (87040150).

References

1 Alastruey, J., Parker, K.H., Peiró, J., et al.: Analysing the pattern of pulse waves in arterial networks: A time-domain study. J. Eng. Math. **64**, 331–351 (2009)
2 Alastruey, J.: On the mechanics underlying the reservoir-excess separation in systemic arteries and their implications for pulse wave analysis. Cardiovasc. Eng. **10**, 176–189 (2010)
3 Avolio, A.P.: Multi-branched model of the human arterial system. J. Med. Biol. Eng. Comput. **18**, 709–718 (1980)
4 Azer, K.: A one-dimensional model of blood flow in arteries with friction, convection and unsteady taylor diffusion based on the womersley velocity profile, [Ph.D. Thesis]. New York University, New York (2006)
5 Formaggia, L., Lamponi, D., Quarteroni, A.: One-dimensional models for blood flow in arteries. J. Eng. Math. **47**, 251–276 (2003)
6 Formaggia, L., Lamponi, D., Tuveri, M., et al.: Numerical modeling of 1D arterial networks coupled with a lumped parameters description of the heart. Comput. Methods Biomech. Biomed. Engin. **9**, 273–288 (2006)
7 Hassani, K., Navidbakhsh, M., Rostami, M.: Simulation of aorta artery aneurysms using active electronic circuit. Am. J. Apll. Sci. **4**, 203–210 (2007)
8 Johnson, D.A., Rose, W.C., Edwards, J.W., et al.: Application of 1D blood flow models of the human arterial network to differential pressure predictions. J. Biomech. **44**, 869–876 (2011)
9 Lee, T.C., Huang, K.F., Hsiao, M.L., et al.: Electrical lumped model for arterial vessel beds. J. Comput. Methods Programs Biomed. **73**, 209–219 (2004)
10 Reymond, P., Merenda, F., Perren, F., et al.: Validation of a one-dimensional model of the systemic arterial tree. Am. J. Physiol. Heart Circ. Physiol. **297**, 208–222 (2009)
11 Sherwin, S.J., Franke, V., Peiró, J., et al.: One-dimensional modelling of a vascular network in space-time variables. J. Eng. Math. **47**, 217–250 (2003)
12 Steele, B.N., Wan, J., Ku, J.P., et al.: In vivo validation of a one-dimensional finite-element method for predicting blood flow in cardiovascular bypass grafts. IEEE Trans. Biomed. Eng. **50**, 649–656 (2003)
13 Steele, B.N., Olufsen, M.S., Taylor, C.A.: Fractal network model for simulating abdominal and lower extremity blood flow during resting and exercise conditions. Comput. Methods Biomech. Biomed. Engin. **10**, 39–51 (2007)
14 Chen, J., Wang, S., Ding, G., et al.: The effect of aneurismal-wall mechanical properties on patient-specific hemodynamic simulations: two clinical case reports. Acta Mech. Sin. **25**, 677–688 (2009)
15 Johnston, B.M., Johnston, P.R., Corney, S., et al.: Non-Newtonian blood flow in human right coronary arteries: transient simulations. J. Biomech. **39**, 1116–1128 (2006)
16 Morbiducci, U., Gallo, D., Massai, D., et al.: On the importance of blood rheology for bulk flow in hemodynamic models of the carotid bifurcation. J. Biomech. **44**, 2427–2438 (2011)
17 Shahcheraghi, N., Dwyer, H.A., Cheer, H.A., et al.: Unsteady and three-dimensional simulation of blood flow in the human aortic archaortic arch. J. Biomech. Eng. **124**, 378–387 (2002)
18 Sheidaei, A., Hunley, S.C., Zeinali-Davarani, S., et al.: Simulation of abdominal aortic aneurysm growth with updating hemodynamic loads using a realistic geometry. J. Med. Eng. Phys. **33**, 80–88 (2011)
19 Tada, S., Tarbell, J.M.: A Computational study of flow in a compliant carotid bifurcation–stress phase angle correlation with shear stress. Ann. Biomed. Eng. **33**, 1202–1212 (2005)
20 Vincent, P.E., Plata, A.M., Hunt, A.A.E., et al.: Blood flow in the rabbit aortic arch and descending thoracic aorta. J. R. Soc. Interface. **8**, 1708–1719 (2011)
21 Zhang, X., Yao, Z., Zhang, Y., et al.: Experimental and computational studies on the flow fields in aortic aneurysms associated with deployment of AAA stent-grafts. Acta Mech. Sin. **23**, 495–501 (2007)
22 Marshall, I., Zhao, S., Papathanasopoulou, P., et al.: MRI and CFD studies of pulsatile flow in healthy and stenosed carotid bifurcation models. J. Biomech. **37**, 679–687 (2004)
23 Giddens, D.P., Zarins, C.K., Glagov, S.: The role of fluid mechanics in the localization and detection of atherosclerosis. J. Biomech. Eng. **115**, 588–594 (1993)
24 Bressloff, N.W.: Parametric geometry exploration of the human carotid artery bifurcation. J. Biomech. **40**, 2483–2491 (2007)
25 Fan, Y., Jiang, W., Zou, Y., et al.: Numerical simulation of pulsatile non-Newtonian flow in the carotid artery bifurcation. Acta Mech. Sin. **25**, 249–255 (2009)
26 Gijsen, F.J.H., van de Vosse, F.N., Janssen, J.D.: The influence of the non-Newtonian properties of blood o the flow in large arteries: steady flow in a carotid bifurcation model. J. Biomech. **32**, 601–608 (1999)
27 Perktold, K., Resch, M., Florian, H.: Pulsatile non-Newtonian flow characteristics in a three-dimensional human carotid bifurcation model. J. Biomech. Eng. **113**, 464–475 (1991)
28 Rindt, C.C.M., van Steenhoven, A.A.: Unsteady flow in a rigid 3-D model of the carotid artery bifurcation. J. Biomech. **118**, 90–96 (1996)
29 Ghalichi, F.: Pulsatile laminar and turbulent blood flow simulation in large stenosed arteries and stenosed carotid artery bifurcation. [PhD Thesis]. Laval University, Quebec (1998)
30 Cheung, S.C., Wong, K.K., Yeoh, G.H., et al.: Experimental and numerical study on the hemodynamics of stenosed carotid bifurcation. Australas. Phys. Eng. Sci. Med. **33**, 319–328 (2010)

31 Long, Q., Xu, X.Y., Ramnarine, K.V., et al.: Numerical investigation of physiologically realistic pulsatile flow through arterial stenosis. J. Biomech. **34**, 1229–1242 (2001)

32 Massai, D., Soloperto, G., Gallo, D., et al.: Shear-induced platelet activation and its relationship with blood flow topology in a numerical model of stenosed carotid bifurcation. Eur. J. Mech. B-Fluid. **35**, 92–101 (2012)

33 Moayeri, M.S., Zendehbudi, G.R.: Effects of elastic property of the wall on flow characteristics through arterial stenoses. J. Biomech. **36**, 525–535 (2003)

34 Stroud, J.S., Berger, S.A, Saloner, D.: Influence of stenosis morphology on flow through severely stenotic vessels: implications for plaque rupture. J. Biomech. **33**, 443–455 (2000)

35 Urquiza, S.A., Blanco, P.J., Vénere, M.J., et al.: Multidimensional modelling for the carotid artery blood flow. J. Comput. Methods Appl. Mech. Engrg. **195**, 4002–4017 (2006)

36 Laganà, K., Balossino, R., Migliavacca, F., et al.: Multiscale modeling of the cardiovascular system: application to the study of pulmonary and coronary perfusions in the univentricular circulation. J. Biomech. **38**, 1129–1141 (2005)

37 Moura, A.: The geometrical multiscale modelling of the cardiovascular system: Coupling 3D and 1D FSI models, [Ph.D. Thesis]. Politecnico di Milano, Milan (2007)

38 Balossino, R., Pennati, G., Migliavacca, F., et al.: Computational models to predict stenosis growth in carotid arteries: which is the role of boundary conditions? Comput. Methods Biomech. Biomed. Engin. **12**, 113–123 (2009)

39 Blanco, P.J., Feijóo, R.A., Urquiza, S.A.: A unified variational approach for coupling 3D–1D models and its blood flow applications. Comput. Methods Appl. Mech. Engrg. **196**, 4391–4410 (2007)

40 Formaggia, L., Gerbeau, J.F., Nobile, F., et al.: On the coupling of 3D and 1D Navier-Stokes equations for flow problems in compliant vessels. Comput. Methods Appl. Mech. Engrg. **191**, 561–582 (2001)

41 Janela, J., Moura, A., Sequeira, A.: Absorbing boundary conditions for a 3D non-Newtonian fluid–structure interaction model for blood flow in arteries. J. Eng. Sci. **48**, 1332–1349 (2010)

42 Liang, F., Fukasaku, K., Liu, H., et al.: A computational model study of the influence of the anatomy of the circle of willis on cerebral hyperperfusion following carotid artery surgery. Biomed Eng Online 10:84 (2011)

43 Nobile, F.: Coupling strategies for the numerical simulation of blood flow in deformable arteries by 3D and 1D models. J. Math. Comput. Mod. **49**, 2152–2160 (2009)

44 Passerini, T., De Luca, M.R., Formaggia, L., et al.: A 3D/1D geometrical multiscale model of the cerebral vasculature. J. Eng. Math. **64**, 319–330 (2009)

45 Qin, K., Jiang, Z., Sun, H., et al.: A multiscale model for analyzing the synergy of CS and WSS on the endothelium in straight arteries. Acta Mech. Sin. **22**, 76–83 (2006)

46 Quarteroni, A., Veneziani, A.: Analysis of a geometrical multiscale model based on the coupling of ode's and pde's for blood flow simulation. Multiscale Model Simul. **1**, 173–195 (2003)

47 Ruan, W.: A coupled system of ODEs and quasilinear hyperbolic PDEs arising in a multiscale blood flow model. J. Math. Anal. Appl. **343**, 778–798 (2008)

48 Sankaran, S., Esmaily Moghadam, M., Kahn, A.M., et al.: Patient-specific multiscale modeling of blood flow for coronary artery bypass graft surgery. Ann. Biomed. Eng. (2012) DOI 10.1007/s10439-012-0579-3

49 Liu, Z.Y., Zhou, Y.S.: A coupling model of left ventricle and arterial system. Acta Mech. Sin. **5**, 285–292 (1989)

50 Formaggia, L., Nobile, F., Quarteroni, A., et al.: Multiscale modelling of the circulatory system: A preliminary analysis. Comput. Visual. Sci. **2**, 75–83 (1999)

51 Quarteroni, A., Ragni, S., Veneziani, A.: Coupling between lumped and distributed models for blood flow problems. J. Comput. Visual. Sci. **4**, 111–124 (2001)

52 Shi, Y., Lawford, P., Hose, R.: Review of zero-D and 1-D models of blood flow in the cardiovascular system. Biomed. Eng. 10:33 (2011)

53 Bharadvaj, B.K., Mabon, R.F., Giddens, D.P.: Steady flow in a model of the human carotid bifurcation. Part I: Flow visualization. J. Biomech. **15**, 349–362 (1982)

54 Rideout, V.C.: Mathematical and Computer Modeling of Physiological Systems. Prentice Hall, NewYork (1991)